International Journal of Solids and Structures
April 2015, Volume 58, Pages 106-116
http://dx.doi.org/10.1016/j.ijsolstr.2014.12.022
http://archimer.ifremer.fr/doc/00245/35647/

Finite element simulation of the mechanical behaviour of synthetic braided ropes and validation on a tensile test

Vu Thanh Do [1, 2], Durville Damien [1, 2, *], Davies Peter [1, 2]

[1] Ecole Centrale de Paris, CNRS UMR8579, Laboratoire de Mécanique des Sols, Structures et Matériaux, 92290 Châtenay-Malabry, France
[2] IFREMER, Centre de Bretagne, Marine Structures Laboratory, 29280 Plouzané, France

* Corresponding author : Damien Durville, email address : damien.durville@ecp.fr ; Peter.Davies@ifremer.fr

Abstract :

A finite element approach to the mechanical behaviour of braided ropes at the scale of their internal components is proposed in this paper. The ropes considered are composed of a few tens of textile yarns, twisted into strands, which are then braided together. The approach aims at determining the mechanical equilibrium of such structures, viewed as assemblies of yarns undergoing large displacements and developing contact-friction interactions. To solve this equilibrium within a quasi-static framework, and using an implicit solution scheme, each yarn of the rope is represented by a finite strain beam model, and special emphasis is put on the detection and modelling of contact-friction interactions between yarns. The approach is used first to determine the unknown initial configuration of the rope, starting from an arbitrary configuration and using contact interactions together with information from the selected braid pattern, to determine the braided structure as the solution of a mechanical equilibrium. Comparisons are made with experimental data on this initial geometry. Tensile test experiments were performed to characterize the mechanical response of both the elementary yarns and the braided rope. These tests were simulated with the model, and results are compared with experiment. Sensitivity analyses on design parameters showing the abilities of the model are reported.

Keywords : Braided rope, Finite element simulation, Contact-friction, Textile structures, Tensile properties

1. Introduction

In recent years, the offshore industry has developed an increasing need for deep sea handling systems, in order to install heavy equipment at depths down to 3000 meters. Beyond around 2000 meters, steel cables become inefficient due to their heavy weight. Braided synthetic ropes appear as an attractive alternative because of their high strength compared to weight and ease of handling. However, these braided ropes exhibit a high sensitivity to damage induced by their repeated passages over the sheaves of traction winches. Damage sustained by the rope as it passes over the sheave is assumed to be mainly induced by contact-friction interactions. These arise both between the rope and the sheave, and between internal components of the rope at different scales, which undergo relative displacements due to the bending of the rope. In order to assess these contact-friction interactions a numerical model of the rope at the scale of its internal components is required.

The braided synthetic ropes considered in this study are made of filaments arranged on three successive levels. At a first level several thousand

filaments are assembled to form yarns. (These yarns may already be an assembly of smaller yarns twisted together and are sometimes termed rope yarns or assembled yarns, but we will not make that distinction here). A few of these yarns are then twisted together to make up strands, and the final braided rope is obtained by interweaving these strands together. The number depends on the braiding machine and the application but 8-, 12- and 16-strand braids are common. In this paper we will focus on a 12-strand braid configuration. The goal of the present paper is to propose a simulation approach, based on the finite element method, able to reproduce the main phenomena characterizing the mechanical behavior of such ropes. Modelling starting from the elementary filament level is out of reach of the simulation because the rope includes tens of thousands filaments, so the proposed model will address the structure of the braided rope at the level of its constitutive yarns, assuming that these yarns can be conveniently represented by homogeneous constitutive models with appropriate characteristics.

Some modelling studies, aimed at better understanding the mechanical behavior of ropes, are available in the literature. Previous studies were based on assumptions about the geometry of the rope components, usually approximated by helices. Analytical developments based on the equilibrium of helical beams allow mechanical properties in tension and bending to be assessed [1], [2, 3]. However, this kind of development is limited by the fact that the actual geometry of braid components is not accurately defined, although this determines to a large extent the contact-friction interactions taking place between them.

The search for a more precise way to determine the actual geometry of

components within the braid has motivated more recent studies based on numerical simulation. For this purpose, components of the braided structure must be represented by appropriate models, and contact-friction interactions between them must be accounted for. Miao et al. [4] used so-called digital elements to represent yarns by series of rods connected by pins. Contact and friction interactions were considered between nodes, and a static relaxation algorithm was used to determine the initial configuration, starting from an initial estimate of the structure. The method was employed to determine the micro-geometry of 3D braided fabrics. Another way of determining the initial geometry of the braided rope is to determine yarn trajectories by analyzing the braiding process. Tolosana et al. [5] proposed a geometrical approach to approximate these trajectories by means of NURBS (Non-Uniform Rational B-splines) following the motion of bobbins within the braiding machinery. These trajectories were then used as supports for 3D finite element models of yarns, and the structure obtained was compacted until reaching the desired void fraction. Pickett et al. [6] proposed a mechanical simulation of the full braiding process, modeling the interlacing of yarns induced by the motion of the bobbins. Due to the large lengths of yarns to be considered to model the process an explicit dynamic simulation code is required to get a reasonable computational time.

Instead of simulating the whole braiding process using a dynamic explicit solver, an alternative method, based on an implicit solution scheme, is proposed here. The principle of the method is to start with an arbitrary configuration which can be easily defined, but which displays large interpenetrations between yarns, and to let contact interactions gradually separate

these yarns, until obtaining a configuration corresponding to a mechanical equilibrium, and fulfilling the selected braid pattern.

Compared to approaches which simulate the actual braiding process, the first advantage of the method is that the input data related to the braiding are very easy to define: instead of having to describe the complex trajectories of bobbins and the geometries of different tools guiding the yarns in the process, only three integer parameters are required to fully determine the braid pattern. Moreover, instead of having to consider yarn lengths which are large enough to cover the distance between the different parts of the braiding machine, the yarn lengths needed in the proposed approach may be much shorter, as they correspond only to the length of the sample to be tested. A last advantage of the method is related to the use of an implicit solver. With an explicit solver, since the time step is determined by the size of the smallest element, a very large number of steps may be needed to simulate the relatively slow braiding process. With the implicit solver employed in the present work, which allows rather large loading increments to be considered, only a few tens of increments are necessary to determine the initial configuration, the mechanical equilibrium being verified at the end of each increment. Such an approach, previously developed for woven fabrics [7, 8, 9], has been extended to the case of braided structures [10]. The finite element approach employed, whose theoretical background is described in [11], solves the mechanical equilibrium of general beam assemblies subjected to large deformations, and developing contact-friction interactions. Emphasis is put on the modeling of yarns by means of finite strain beam elements, and on the detection and modeling of contact-friction interactions between

yarns. The treatment of very large initial penetrations and the application of appropriate periodic boundary conditions to avoid perturbations of the solution at the ends of the studied samples, are the main difficulties faced in adapting this general approach to the case of braided ropes.

The paper is organized as follows. Section 2 recalls the basic assumptions of the proposed finite element approach. Section 3 describes the method to determine the unknown initial configuration of the braided structure starting from an arbitrary configuration. Experimental tests on individual yarns and on the braided rope are presented in Section 4. Results from a simulation of the tensile test, comparisons with experimental data and sensitivity analyses are reported in Section 5.

2. Description of the finite element approach

The general approach followed by the in-house finite element code used for this study to simulate the mechanical behaviour of fiber assemblies is briefly presented in this section (the reader is referred to [11] for a detailed presentation). The adaptations of this approach, particularly needed for the determination of the unknown initial configuration of braided structures, are the subject of the next section.

2.1. General presentation

The proposed finite element approach aims to determine the mechanical equilibrium of assemblies of fibers undergoing large displacements and developing contact-friction interactions between them. The problem is set in the form of a principle of virtual work, and solved using an implicit solver.

2.2. Modeling of yarn behavior

Each yarn of the assembly is represented using a 3D finite strain beam model able to consider planar deformation of beam cross-sections. According to this model, the position of any particle , identified in the material configuration of the beam by its transversal coordinates ξ_1 and ξ_2, and its longitudinal abscissa ξ_3, is described as follows by three independent kinematical vectors defined on the line of centroids of the fiber:

$$\mathbf{x}(\xi_1, \xi_2, \xi_3) = \mathbf{x}_0(\xi_1 3) + \xi_1 \mathbf{g}_1(\xi 3) + \xi_2 \mathbf{g}_2(\xi 3). \tag{1}$$

In this expression $\mathbf{x}_0(\xi_1 3)$ stands for the position of the center of the cross-section, and $\mathbf{g}_1(\xi 3)$ and $\mathbf{g}_2(\xi 3)$ are two section directors. No constraints are set on these directors, and the variations of their norms and of the angle they form allow planar deformations of cross-sections to be accounted for. A full three-dimensional constitutive law can be used, thanks to the consideration of cross-section deformations.

2.3. Modelling of contact-friction interactions

The detection and modeling of contact interactions which can occur at many locations in the general assembly of fibers is a crucial task for the simulation of such media. The reader is referred to [11] for more details on how to perform this task.

2.3.1. Construction of discrete contact elements

The choice has been made to take into account contact interactions at discrete contact elements distributed along contact zones in the assembly. A contact element is defined as a pair of material particles located on the surface

of interacting yarns, which are predicted to be likely to enter into contact. The detection of contacts and the construction of contact elements can be time consuming due to the large number of yarns considered. To optimize the process, a first stage in the contact detection consists of coarsely delimiting proximity zones between pairs of yarns. A proximity zone is defined as a pair of intervals of curvilinear abscissa defined on the lines of centroids of interacting yarns, the distance between any pair of points belonging to both intervals being lower than a given distance threshold. These proximity zones are determined by evaluating the distance between control points distributed with a coarse discretization size on one of both yarns, and their associated closest points on the opposite yarn (see Figure 1).

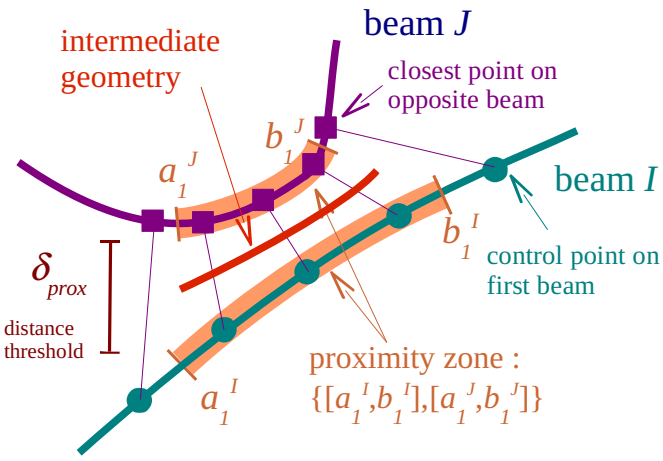

Figure 1: Determination of a proximity zone and its associated intermediate geometry

The construction of proximity zones has two advantages. It provides first a rough localization of contacts within the assembly of yarns, at an affordable

cost. More important, it allows the geometry of the actual contact zone to be approximated through so-called intermediate geometries, defined as the average between both parts of yarns constituting the proximity zone. These intermediate geometries are then used as a geometrical support to generate the contact elements. These contact elements are generated at discrete contact checking locations distributed on each intermediate geometry, with a given discretization size. At each contact checking location on an intermediate geometry, identified by its curvilinear abscissa ζ_i, a contact element, denoted $E_c(\zeta_i)$ is defined as the pair of material particles located on the surfaces Γ_1 and Γ_2 of both interacting yarns (see Figure 2), which can be predicted to enter into contact at this location:

$$\begin{aligned} E_c(\zeta_i) = \{\boldsymbol{\xi}_i^1, \boldsymbol{\xi}_i^2\} \in \Gamma_1 \times \Gamma_2, \text{ such that} \\ \boldsymbol{\xi}_i^1 \text{ and } \boldsymbol{\xi}_i^2 \text{ are predicted to enter into contact at } \mathbf{x}_{int}(\zeta_i), \end{aligned} \quad (2)$$

where $\mathbf{x}_{int}(\zeta_i)$ is the current position of the contact checking point on the intermediate geometry.

Contact search directions used to select these particles are defined from the intermediate geometry, which appears more suitable than directions usually defined as orthogonal to only one of both contacting bodies. The discretization size between contact elements is chosen depending on the finite element discretization size of yarns, so that the number of contact elements remains consistent with the interpolation of displacement fields. However, particles constituting contact elements may be located anywhere with respect to the finite element mesh, and not only at nodes or some other integration points, which allows very different configurations of contact, ranging from contact between parallel yarns to contact between orthogonally crossing

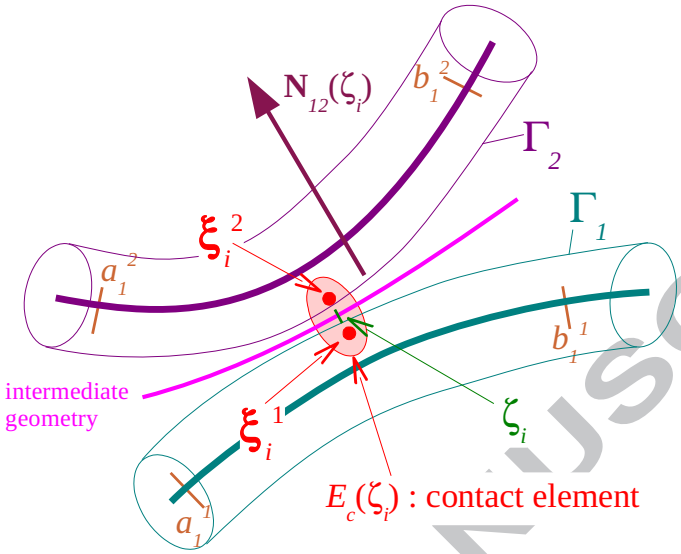

Figure 2: Contact element defined at a given abscissa on the intermediate geometry

yarns, to be considered. Leech has emphasized the importance of considering the large number of contact possibilities in ropes [12].

2.3.2. Expression of the gap function at contact elements

The gap function for a contact element is defined by the distance between the pair of particles forming the element, measured according to a normal contact direction denoted $\mathbf{N}_{12}$, and defined at this contact element:

$$\text{gap}(E_c(\zeta_i)) = \left(\mathbf{x}^2(\boldsymbol{\xi}_i^2) - \mathbf{x}^1(\boldsymbol{\xi}_i^1), \mathbf{N}_{12}(E_c(\zeta_i))\right). \tag{3}$$

The normal direction $\mathbf{N}_{12}$ is computed according to geometrical criteria in order to be oriented in the best way to prevent both yarns from crossing through each other.

2.3.3. Models for normal and tangential reactions

Contact is modeled using a regularized penalty method in order to exert opposite reaction forces on both particles of a contact element when a penetration is detected. These reaction forces are assumed to evolve linearly with the penetration for sufficiently large penetrations, but are taken proportional to the square of the penetration for very small penetrations belong a regularization threshold. According to this strategy, the normal reaction R_N is expressed as function of the penetration gap in the following way:

$$\begin{cases} \text{if } \text{gap} > 0, R_N = 0, \\ \text{if } -p_{reg} \leq \text{gap} \leq 0, R_N = \dfrac{k_c}{2p_{reg}} \text{gap}^2, \\ \text{if } \text{gap} < -p_{reg}, R_N = -k_c \left(\text{gap} + \dfrac{p_{reg}}{2}\right), \end{cases} \tag{4}$$

where k_c is the penalty coefficient and p_{reg} the regularization threshold. This quadratic regularization ensures a continuity of the normal stiffness when the penetration vanishes, thus stabilizing the transition between contacting and non-contacting status. The penalty coefficient is automatically adapted locally for each proximity zone in order to control the maximum penetration registered on each contact zone. A regularized friction model, allowing a small reversible tangential relative displacement before large scale sliding occurs, is considered to represent tangential reactions. Denoting $\mathbf{g}_T$ the tangential relative displacement, the tangential $\mathbf{R}_T$ is expressed as follows:

$$\begin{cases} \text{if } \|\mathbf{g}_T\| \leq g_{rev,max}, \mathbf{R}_T = \mu \left|R_N\right| \dfrac{\mathbf{g}_T}{g_{rev,max}}, \\ \text{else } \mathbf{R}_T = \mu \left|R_N\right| \dfrac{\mathbf{g}_T}{\|\vec{g}_T\|}, \end{cases} \tag{5}$$

where $g_{rev,max}$ is the maximum allowed reversible tangential displacement.

2.4. Modelling of boundary conditions

The definition of boundary conditions at the ends of the different level subcomponents is an important issue when dealing with fibre assemblies. Prescribing displacements at ends of these components is necessary to ensure the mechanical problem is well posed, but on the other hand, allowing ends of subcomponents the possibility of rearranging is also required to take into account the deformability of the structure at its boundaries. To meet these competing needs, boundary conditions are controlled by associating rigid bodies to the ends of subcomponents of different levels, and by formulating averaged conditions for groups of ends, in accordance with the hierarchical arrangement of the rope into yarns, tows, layers and global structure.

In the case of periodicity conditions, relationships between opposite ends can be established and prescribed, so that the usual perturbations induced by conditions at ends disappear, as will be shown in the examples presented in this study.

3. Determination of the initial configuration of braided ropes by gradual separation of yarns

A way of using the modeling of contact-friction interactions within fiber assemblies described above, to determine the initial geometry of braided structures, is presented in this section. Starting from a first easily available approximation of the braid structure, defined by simple geometrical functions, but allowing unrealistic interpenetrations between yarns, this modelling of contact interactions is used together with information related to the relative stacking of yarns within the braid, to gradually reduce penetrations

between yarns until obtaining an equilibrium configuration in agreement with the selected braiding pattern.

3.1. Principles

Although trajectories of yarns within the braid cannot be easily determined a priori, two kinds of information are however available. Correspondingly with the global helical arrangement of the rope, a first rough approximation of the geometry of tows can be made by helices characterized by their twist pitch and their radius. In addition, the selected braiding pattern specifies, at each crossing between tows, which tow should be above or below the other. Mixing this information, the principle of the proposed approach is to start from a configuration where tow and yarn trajectories are respectively described by simple and double helices, but which displays large inter-penetrations between intersecting yarns, and to use the stacking order defined by the braiding pattern to orient contact interactions in order to move inter-penetrating yarns away from each other. Applying this method, initial penetrations between yarns are very large compared to their radii, which raises difficulties regarding the convergence of contact algorithms. Adapting the orientation of the normal contact direction and gradually reducing the gap at contact elements are two improvements to the usual contact algorithms that enable the determination of the initial configuration.

3.2. Adaption of the normal direction

In the standard contact algorithm, the normal contact direction, entirely defined by the relative positions of contact particles and by the local geometry of interacting beams, determines the orientation according to which these

particles are not allowed to inter-penetrate. Consequently, a particle initially located above another will be forced, by contact conditions, to remain on the same side defined by the normal contact direction. However, when determining the initial configuration, the repulsion direction should not be determined by the relative positions of particles, but by the stacking order prescribed by the weaving pattern. For the repulsion direction to be in accordance with the braiding pattern, the sign of standard normal contact direction is simply changed depending on the stacking order between the crossing tows.

3.3. Gradual reduction of contact gaps

Attempting to reduce large initial penetrations between yarns in only one step induces instabilities that prevent the convergence of contact algorithms. To stabilize contact algorithms, gaps are gradually reduced step by step during the determination of the initial configuration according to the following algorithm, by defining a maximum gap reduction per increment, denoted $\delta\,\mathrm{gap}_{max}$. Let gap^{ini} denote the value of the gap for a given contact element at the beginning of the step. The principle of the gradual reduction of the gap is to retain as the value of the gap to be considered to calculate the normal reaction using Eq. 4, the difference between the actual gap and the initial one, reduced by the allowed gap variation $\delta\,\mathrm{gap}_{max}$ (see Fig. 3). Instead of using the standard gap to evaluate the normal reaction, this reaction is calculated using a modified gap, denoted gap^{*} and defined as follows:

$$\begin{cases} \text{if } \ \mathrm{gap} \geq \mathrm{gap}^{ini} - \delta\,\mathrm{gap}_{max}, \mathrm{gap}^{*} = \mathrm{gap}, \\ \text{else } \ \mathrm{gap}^{*} = \mathrm{gap} - \left(gap^{ini} - \delta\,\mathrm{gap}_{max}\right). \end{cases} \tag{6}$$

In this way, for each loading increment, the variation of the gap at every contact element is limited by the parameter $\delta\,\mathrm{gap}_{max}$, which allows the rate

of the separation between yarns to be controlled.

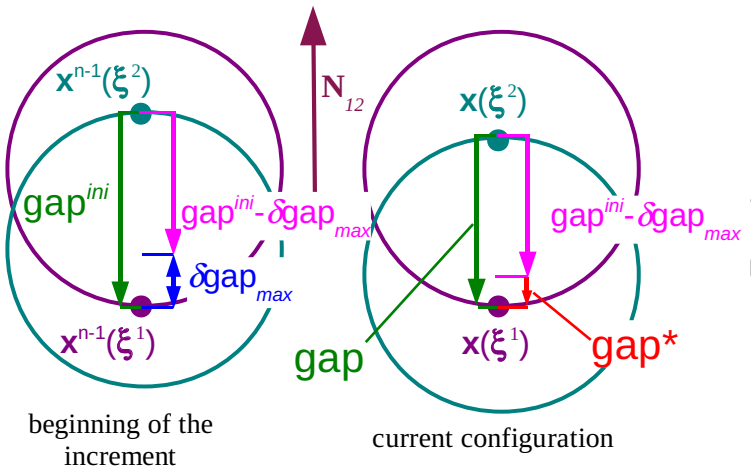

Figure 3: Definition of the modified gap used for the process of gradual reduction of gaps

The standard contact algorithm is applied once the initial configuration has been computed.

3.4. Application to the case of braided ropes

To apply this gradual separation process to the case of braided ropes, we need to define the first approximation of the geometry to start from, and to determine the stacking order at each crossing between yarns from the definition of the selected braiding pattern.

3.4.1. Definition of the arbitrary starting configuration

Yarns within a braided rope are arranged according to two successive levels. They are first twisted to form elementary strands, which are themselves braided together. As arrangements at both levels are characterized by a pitch

length and a mean radius around a revolution axis, we propose to define the yarn trajectories in the first starting approximation for the braid geometry by double helices.

The geometrical parameters needed to define this configuration are the helix pitch p_{strand} and the helix radius ρ_{strand} for strands, and the helix pitch p_{yarn} and the helix radius ρ_{yarn} for yarns within the strand, together with the radius of yarns r_{yarn} (see Figure 4a). In order to have a periodic structure, the length of the starting configuration is taken as a multiple of the strand helix pitch p_{strand}, which should itself be a multiple of the yarn helix pitch p_{yarn}.

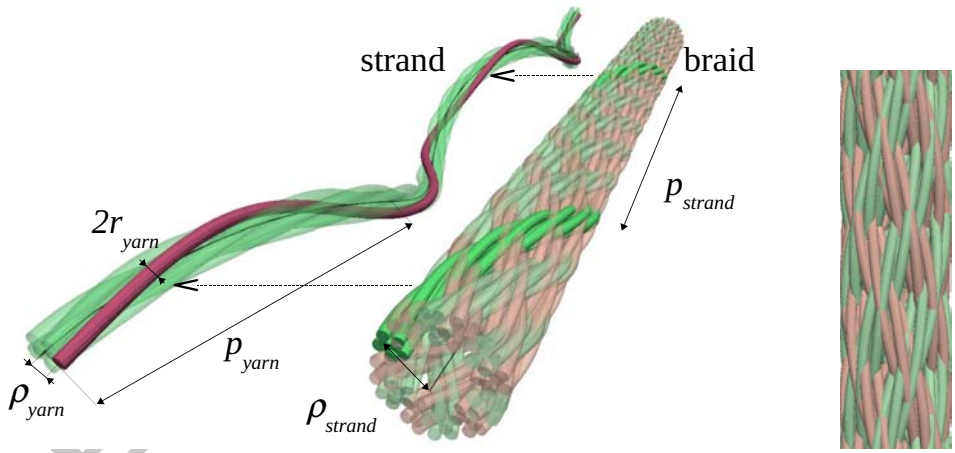

(a) (b)

Figure 4: a: Geometrical parameters defining the double helices of yarn trajectories in the arbitrary starting configuration; b: Detail of the starting configuration showing initial interpenetration between yrans

3.4.2. Taking into account the braid pattern

With the description of the starting configuration above, the strands from different layers are inter-penetrating each other. Based on the braid pattern at each crossing, it is possible to determine which strand is below or above the other at the crossing between two layers. The elementary motif, consisting of superposed layers, is periodically repeated. For the rope considered in this study, a strand passes twice over then twice under the strand of another layer with a shift of 1 in the same layer (called braid pattern). Further, a couple of strands from two layers will meet twice in a period according to the change of their relative position, and a strand will also intersect each strand from another layer twice, with possibly different stacking orders (Figure 5). Therefore, the elementary motif is the two-dimensional matrix, in which the size is twice the number of strands per layer. The stacking order is determined by the function Braid_pattern(s_1, s_2), taking its value in $\{-1, +1\}$, s_1 and s_2 standing for the numbers of the strands from both layers relatively to the elementary motif, Figure 6.

Now, we take back any intersection between two yarns y_a and y_b, belonging to two different strands s_a and s_b from both layers, to the elementary motif (Figure 6). In the cylindrical coordinate system (ϕ, z), the vectors which decide the shift between two intersections of a couple of strands are $\boldsymbol{D}_1 = (180°, \frac{p_{strand}}{2})$ and $\boldsymbol{D}_2 = (-180°, \frac{p_{strand}}{2})$. The direction of each vector corresponds to that of a layer of assembled yarns and the length measures the distance between two intersections (same state of superposition) of a pair of assembled yarns. Now we determine the superposition of a pair of strands at a given crossing. A crossing point belonging to strand 1 and strand 2,

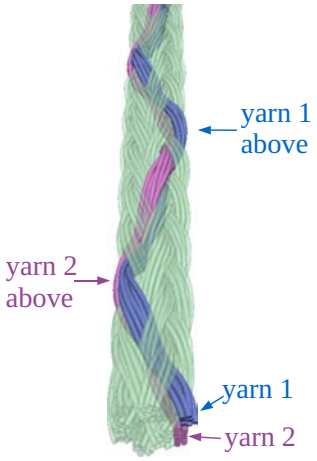

Figure 5: Alternate stacking order at successive crossings between two yarns

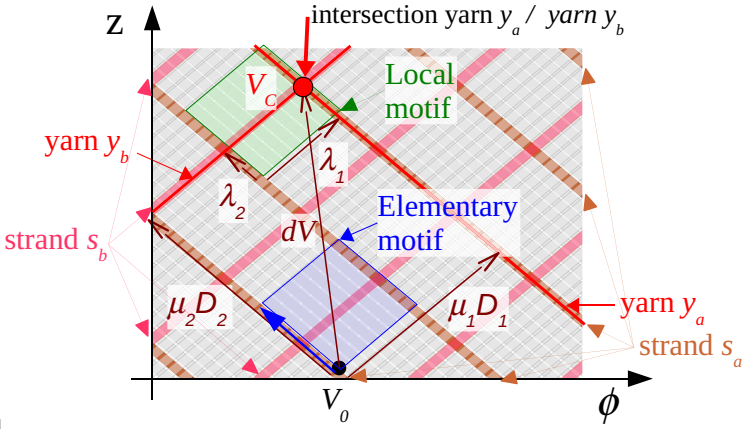

Figure 6: Determination of the stacking order at the intersection between two crossing yarns: same strands intersect repeatedly with different stacking orders depending on their position with respect to the local motif

is described by the vector $\boldsymbol{V}_c$ in the plane (ϕ, z). The difference between this vector and the vector at the first intersection is $\boldsymbol{dV} = \boldsymbol{V}_c - \boldsymbol{V}_0$. The

components (μ_1, μ_2) of $\boldsymbol{dV}$ in $(\boldsymbol{D}_1, \boldsymbol{D}_2)$ are calculated:

$$\boldsymbol{dV} = \mu_1 \boldsymbol{D}_1 + \mu_2 \boldsymbol{D}_2.$$

These components (μ_1, μ_2) are changed into integer values (μ_1^*, μ_2^*) in the following way:

$$\mu_1^* = \text{Floor}(\mu_1 + \frac{1}{2}),\ \mu_2^* = \text{Floor}(\mu_2 + \frac{1}{2}),$$

where Floor($\bullet$) denotes the floor function, giving, for a real value, the highest integer which is lower than this value. Integer components with respect to the local elementary motif, denoted (λ_1, λ_2), are then obtained by taking these values modulo 2:

$$\lambda_1 = \mu_1^* - 2 \times \text{Floor}(\frac{\mu_1^*}{2}),\ \lambda_2 = \mu_2^* - 2 \times \text{Floor}(\frac{\mu_2^*}{2}).$$

Finally, the stacking order between yarns y_a and y_b, belonging to strands s_a and s_b is determined using the braid pattern function:

$$\text{Stacking\_order}(y_a, y_b) = \text{Braid\_pattern}(s_a + \lambda_1 \times N_1, s_b + \lambda_2 \times N_2),$$

where N_1 and N_2 are the numbers of strands in the first and second layer of the braid.

3.4.3. Boundary conditions at ends

During the determination of the initial configuration, considering a periodic sample, periodic boundary conditions are prescribed in transverse directions to the rope. In the longitudinal direction, displacements are fixed at one end of the rope, while all yarns are connected, at the other end, to the same rigid body, to which is a small tensile force is applied.

3.4.4. Gradual reduction of initial gaps for the determination of the initial configuration

According to the process described above, yarns, initially strongly interpenetrating each other in the arbitrary starting configuration, are gradually moved away from each other by the actions of contact-friction interactions, which have been reoriented in order to fulfill the stacking order defined by the braid pattern, as shown in Figures 7 and 8. This rearrangement process results in deformations in yarns, mainly in terms of elongation, bending and torsion, which are taken into account by the beam model employed. This way, the initial configuration is obtained as the solution of a mechanical equilibrium.

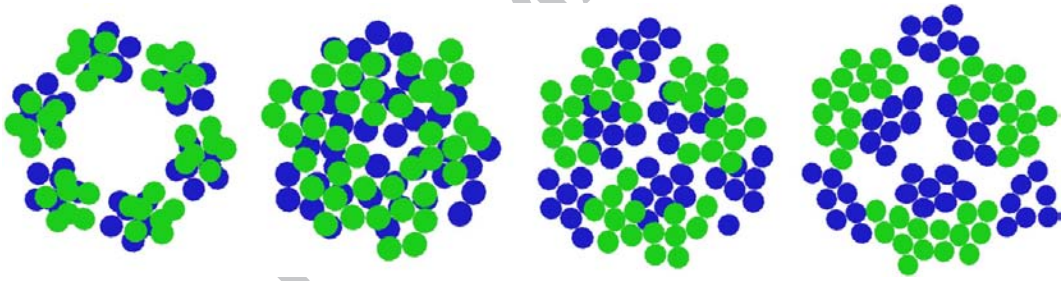

Figure 7: Cross-section at the successive steps during the determination of the initial configuration of the braided rope

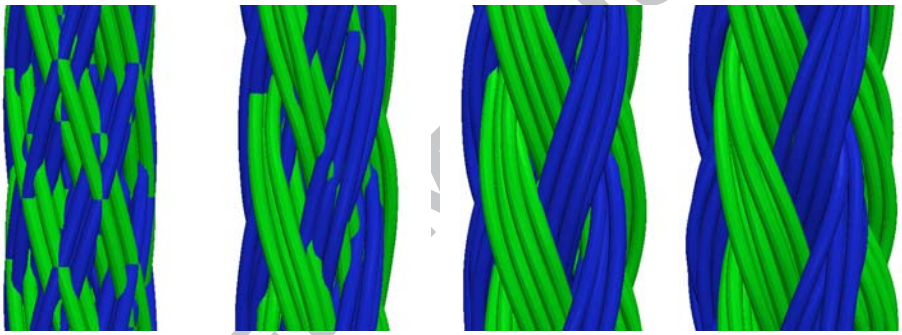

Figure 8: Evolution of the shape of the rope at the successive steps during the determination of its initial configuration

4. Experimental tests

Experimental tests were carried out to identify the mechanical properties both at the level of a braided rope, and at the level of individual yarns making up this rope. Axial stiffnesses identified on individual ropes are used as input data for the numerical model. The force/strain curve experimentally obtained for the considered rope will be compared to the one resulting from simulation.

4.1. Layout of the rope

The ropes considered in this study are AmSteel Blue^{TM} braids manufactured by Samson. They are made of 12 strands, arranged into two layers of 6 strands each. All strands are identical, and made of 7 twisted yarns. The fibre material is HMPE (high modulus polyethylene).

4.2. Yarns

4.2.1. Test procedure

Tensile tests were performed on an Instron 10 kN capacity electro-mechanical test frame. Samples were extracted from a rope section. Their lengths and weights were measured accurately. They were then placed in special pneumatic clamps which limit end stress concentrations. A small preload (5-10 N) was applied to tension the sample and measure the initial length. The distance between clamps was 300mm.

Elongations were measured using an in-house video extensometry system based on two digital cameras. Two black markers are attached to the sample and the cameras follow their movement. The initial distance between the markers, L_0, is measured and image analysis software enables the strain to

be determined. Load is also recorded continuously. The loading rate was 10 N/s.

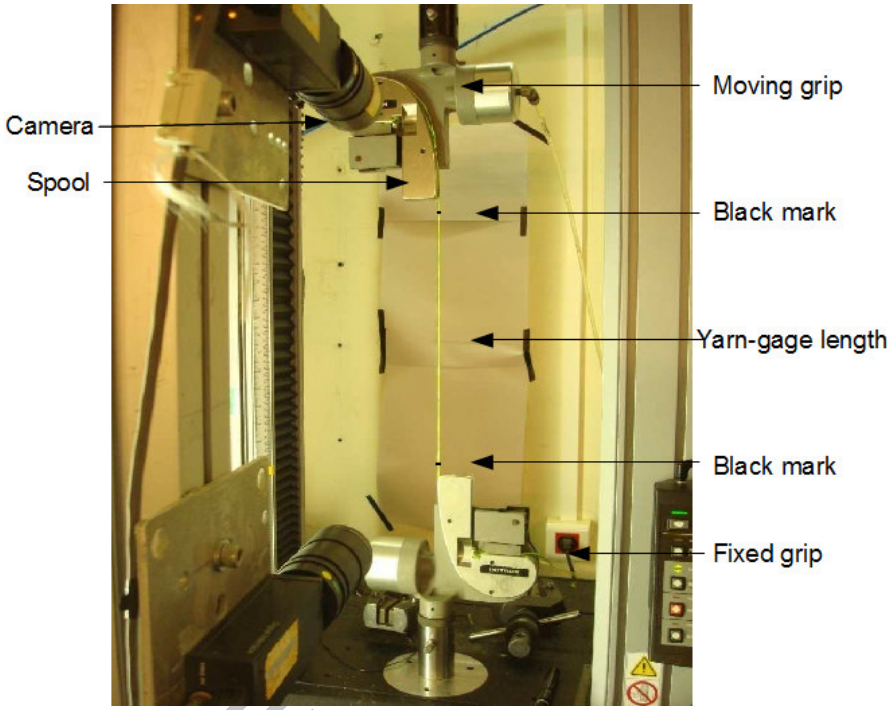

Figure 9: Experimental setup for identification of tensile properties of yarns

4.2.2. Test results

Two types of test were performed on yarns. In the first, the samples were simply loaded directly to failure (Figure 10a). In the second, 5 bedding-in cycles were applied at a load of 600N and then the sample was loaded to failure (Figure 10b). Table 1 summarizes the results. A mean curve was constructed by determining the mean force value from all the tests at each strain value.

Initially (01.2% strain), the slope is concave. As the load increases the

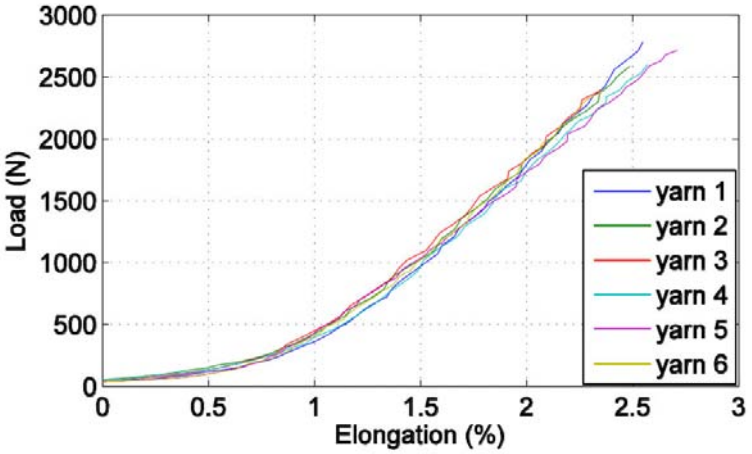

(a) Tensile tests with straight ramp to failure

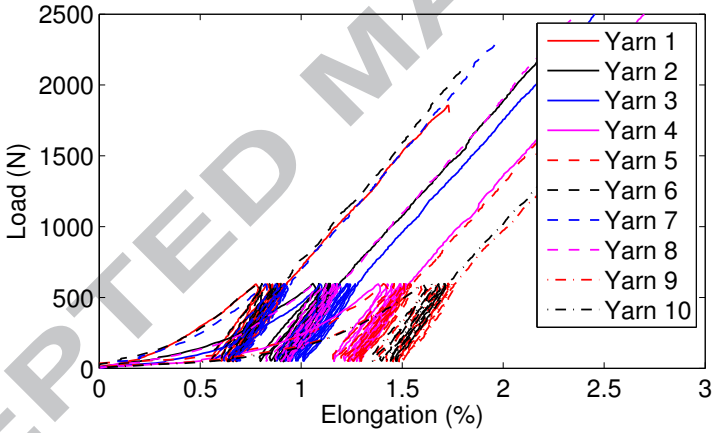

(b) Tensile tests with bedding-in cycles

Figure 10: Examples of results from tensile tests on yarns

fibres become more organized. The bedding-in of the fibres in this initial region is due to both a molecular reorientation within the fibres, and a reorientation of the fibres in the yarns [13]. Beyond this region the curve becomes linear and the slope is defined by a least squares adjustment. Yarn cross sec-

tional areas may be estimated by evaluating experimentally their mass per unit length, and by dividing this lineic density by the volumic density of the material. For the samples studied, a typical value of 2.06 mm^2 is obtained. Because of the difficulty in defining the cross-section of the yarns, the axial stiffness (EA) is determined rather than Young's modulus, Table 1.

Failures were observed to occur both near the sample ends and in the central section, no significant difference was noted for strengths corresponding to the two failure locations.

	No bendding-in	After bedding-in cycles
Number of tests	6	11
Average axial stiffness (kN)	161	162
Standard deviation (kN)	6	4

Table 1: Identified stiffness characteristics of yarns

4.3. Braided ropes

4.3.1. Test procedure

The rope tests were performed on a 1000 kN capacity 10 meter long hydraulic test machine. Samples were 8 meters long and terminated with spliced loops, which were placed over 100mm diameter loading pins at each end of the test frame, Figure 11. Elongations were measured using the same in-house video extensometry system based on two digital cameras as for the yarn tests. In this case the cameras were mounted on a rail above the test machine. Loading rate was 20% of break load per minute. This is the same global rate as for the yarn samples, although the yarns in the rope will

see a slightly lower rate, depending on their location, due to the angular construction. During the first loading the orientations cause a stiffening effect. The transverse section stabilizes progressively under load. Also, when load-unload cycles were applied before the break tests both hysteresis and plastic behavior was noted.

Figure 11: Test frame for rope tests. Left: Overview showing cameras above test frame. Right: Rope in place during test.

4.3.2. Test results

Load-elongation plots from four rope tests are shown in Figure 12. Figure 12a shows one direct and three tests with 5 cycles of load-unload, while Figure 12b shows the first and last bedding-in cycles of one of these tests. The hysteresis observed on the curves may be due both to material effects, similar to those displayed on yarns (Figure 10b), and to dissipation by friction induced by a gradual rearrangement of yarns. The hysteresis tends to decrease with number of bedding-in cycles, most of the residual strain is removed during the first cycle, and the form of the curve then becomes more

linear. The stiffness of rope was calculated based on the linear part of the final curve, Table 2.

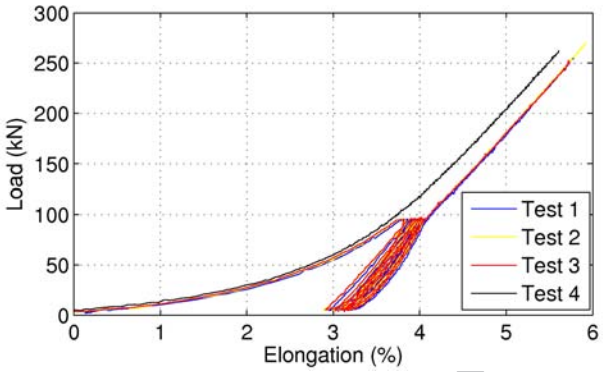

(a) One direct test and three with bedding-in

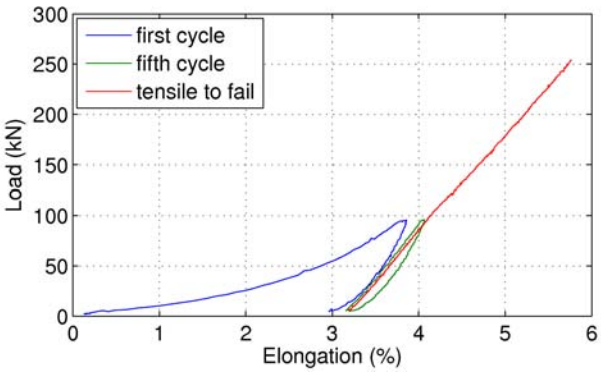

(b) Detail of test showing first and last bedding-in cycles

Figure 12: Tensile tests on braided rope samples

4.4. Relationship between yarn and rope stiffness

The effect of the braiding and twisting is demonstrated by the reduction of the axial stiffness between the two scale levels of the structure, yielding a

Number of specimens	4
Average axial stiffness (kN)	9512
Standard deviation (kN)	82.3

Table 2: Identified stiffness characteristics of braided rope

transfer coefficient of stiffness from yarn to rope of around 70%.

$$C_{eff} = \frac{K_{braid}}{n_{yarn} \times K_{yarn}} = \frac{9512}{12 \times 7 \times 162} \approx 0.0699.$$

5. Simulation results

5.1. Modeling at the level of elementary yarns

The braided synthetic ropes considered here are composed of filaments arranged into components of two levels, respectively yarns and strands, before forming the rope. In order to model the yarns, made of bundles of filaments, they are assumed to deform as a continuous and homogeneous medium. Some corrections to the 3D constitutive model are needed to account for the fact that the bending and torsional stiffness of yarns are much lower than those of an equivalent solid material, due to the relative motions allowed between filaments. For this reason, the stiffness terms involving the moment of inertia of yarn cross-sections are multiplied by a correction factor taking into account their multi-filamentary structure. In first approximation, neglecting friction effects between fibres, bending and torsional stiffnesses of a bundle of fibres can be estimated by taking the corresponding stiffnesses of an equivalent beam, made of the same material, with an equivalent cross-sectional area, and by dividing these stiffnesses by the number of fibres in the

bundle. The correction factors used have been taken approximately equal to the inverse of the number of filaments constituting the yarns. The value of the Young's modulus of yarns is determined by dividing the axial stiffness (EA) experimentally identified to be 162 kN (Table 1), by the area of the cross-section of beams considered in the model.

5.1.1. Rope architecture

The rope samples studied are made of 12 strands, divided in 2 layers, each strand consisting of 7 yarns (figure 13), making a total of 84 yarns. The length of the samples modelled was taken twice the pitch of the rope.

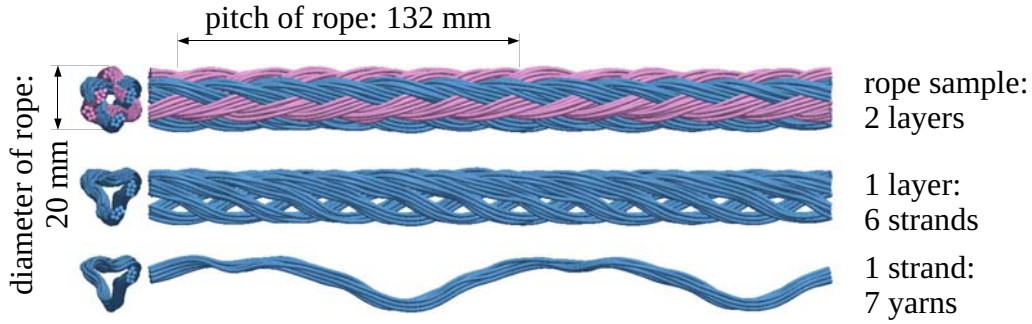

Figure 13: Architecture and dimensions of the rope samples studied

5.1.2. Geometrical validation

Two comparisons were made based on geometry to validate the numerical model. The main geometrical features of the real sample and the model sample are compared in Table 3. The geometrical parameters defining the arbitrary starting configuration are fitted so as to obtain a good agreement between the actual and the modeled samples.

	Real sample	Model sample
Diameter of yarn (mm)	0.83	0.86
Diameter of rope in tension (mm)	19.0	20.0
Pitch of rope (mm)	132	132

Table 3: comparison of geometrical features between the real and the modeled samples

The comparison between a cross-section of the rope obtained by X-ray tomography and a cross-section of the initial configuration resulting from simulation provides a second qualitative validation (Figure 14). Similar voids are observed in the central area of the rope.

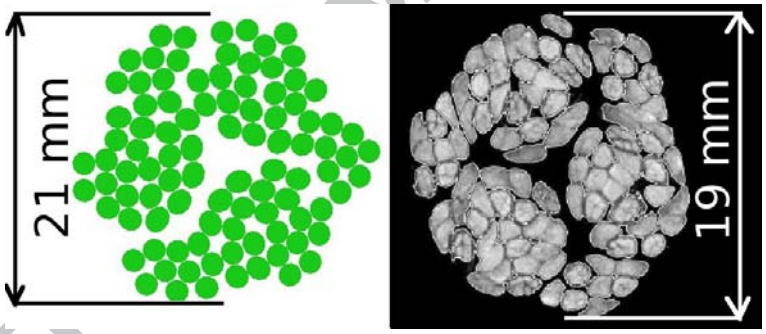

Figure 14: Comparison between a cross-section of the initial configuration determined by simulation and an X-ray tomography image of the rope

5.2. Simulation of a tensile test

5.2.1. Comparison with experimental data

A tensile test was simulated by applying an incremental displacement to the end of the modeled sample, after having determined its initial config-

uration. The force/elongation curve, resulting from simulation, is plotted in Figure 15, and compared with experimental data. Good agreement is obtained for the axial stiffness in the linear part of the curves. The axial stiffness determined from simulation was 9880 KN whereas the mean value identified by experiment was 9512 KN (values from all 4 rope tests).

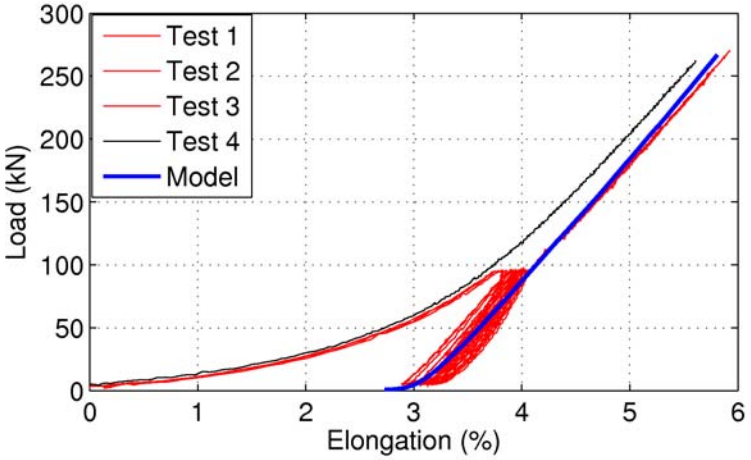

Figure 15: Comparison between force/elongation curves obtained experimentally and by simulation

5.2.2. Axial stresses in yarns

Axial stresses at the scale of individual yarns (Figure 16), derived from simulation, show a large heterogeneity, first between yarns, and second along each yarn. This heterogeneity in axial stresses results both from variations of the local curvatures of yarns and from load transfer between yarns induced by tangential friction interactions. The friction coefficient was taken equal to 0.1, in agreement with values between 0.08 and 0.11 for friction of HMPE fibers on steel reported in [14].

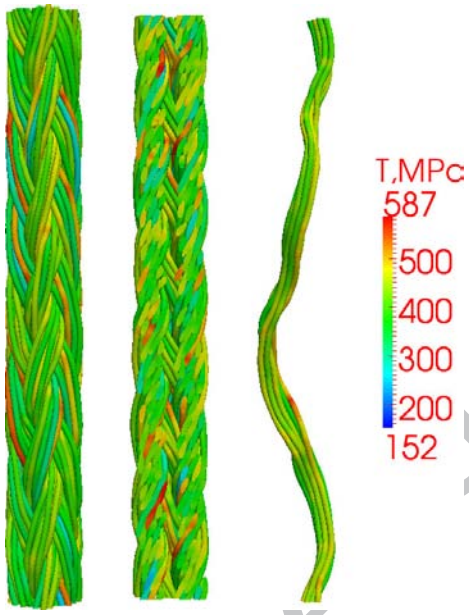

Figure 16: Axial stresses in yarns within a rope subjected to a 70 kN load from left to right; global view of the rope, section along the rope, and view of an individual strand

5.2.3. Parameter sensitivity analysis

Helix pitch length. The axial stiffness of the rope depends on the local orientation of yarns with respect to the rope axis. An efficiency coefficient C_{eff}, evaluated by dividing the axial stiffness of the rope by the sum of the axial stiffnesses of yarns, can be used to characterize this effect. The average elongation of yarns is related to the rope elongation through a coefficient $\cos\alpha$, where α is the helix angle of strands, whose tangent can be calculated as a function of the strand helix radius ρ_{strand} and the strand helix pitch p_{strand} as:

$$\tan\alpha = 2\pi\frac{\rho_{strand}}{p_{strand}}.$$

Since the contribution of each yarn to the load in the axial direction of the rope is affected by a coefficient $\cos\alpha$, the axial stiffness of the rope should evolve linearly with the coefficient $(\cos\alpha)^2$. To verify this effect, the same procedure (determination of the initial configuration and simulation of a tensile test) was applied to four different samples, only varying the strand helix pitch. Figure 17 shows an example of the sections for 3 pitch angles. The evolution of the rope axial stiffness with the coefficient $(\cos\alpha)^2$, plotted in Figure 18, shows a linear relationship.

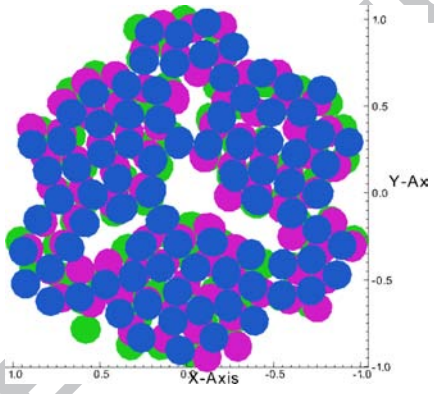

Figure 17: Section through braided ropes with three pitch lengths, (green 121mm, violet 131mm, blue 153mm)

Friction coefficient. A sensitivity analysis was also performed to examine the influence of the friction coefficient between yarns on the response of the rope. This coefficient affects load transfers between yarns, and consequently the axial stresses distribution. The same tensile test simulation was run with three different values of the friction coefficient between yarns: 0.003, 0.03 and 0.1. The corresponding loading curves are plotted in Figure 19. The variation of the friction coefficient influences only the beginning of the curve correspond-

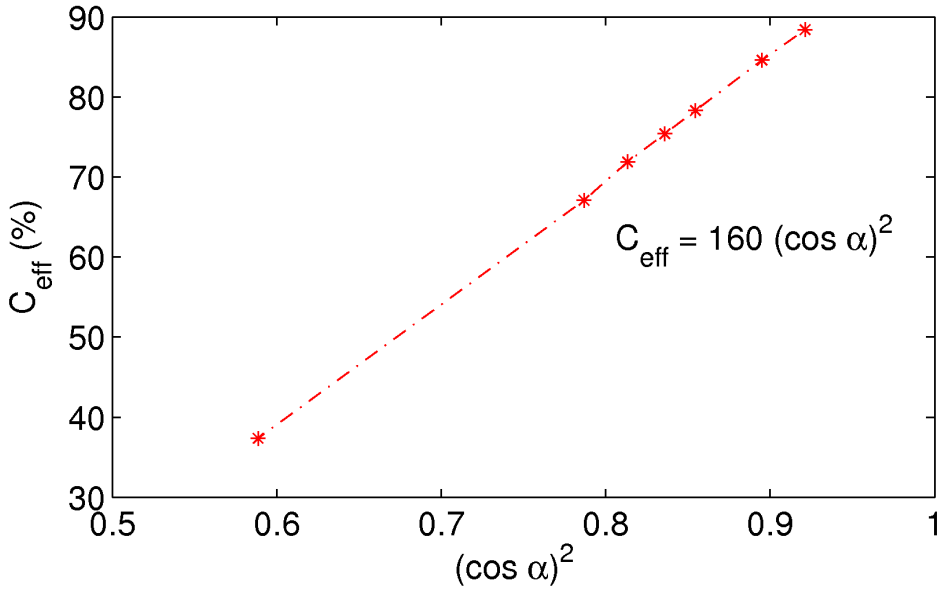

Figure 18: Evolution of the rope axial stiffness with the $(\cos \alpha)^2$ coefficient

ing to nonlinear geometrical effects: the increase of the friction coefficient reduces the ability of yarns to rearrange in order to fill voids between them. However, once these initial gaps between yarns have vanished, the rope axial stiffness no longer depends on the friction coefficient, which suggests that friction has little influence on this tensile behaviour. The friction coefficient has nevertheless a large influence on the stress distribution among yarns, as shown in Figure 20. There is a much larger variability in loads when the friction coefficient is higher, which can be explained by non-uniform load transfers between yarns resulting in local stress concentrations. The friction coefficient will therefore be expected to affect damage development and failure load.

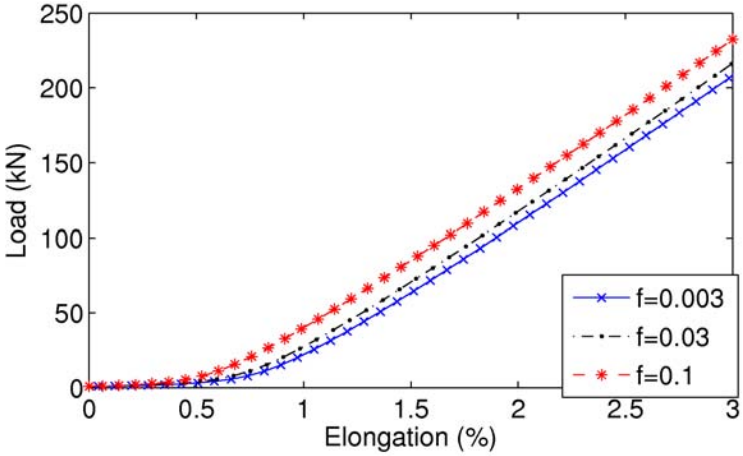

Figure 19: Loading curves for the tensile test simulation with three different friction coefficients

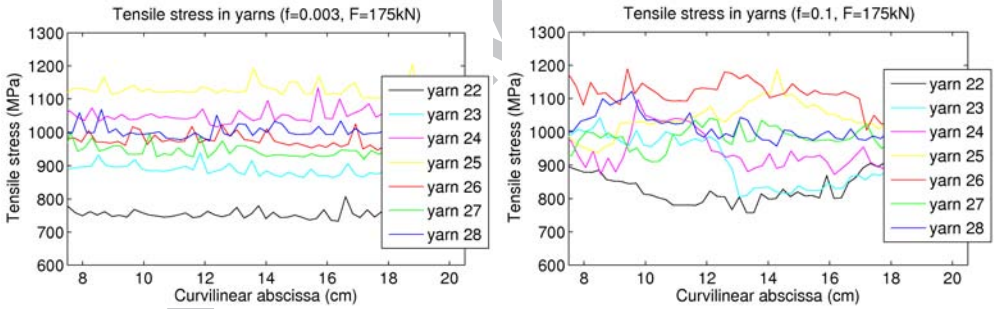

Figure 20: Stress distributions among yarns for the tensile test with two different friction coefficients, 0.003 and 0.1

6. Conclusion

A numerical model of braided ropes has been proposed, which takes into account contact-friction interactions between elementary components within a large deformation framework. The approach is first employed to determine the unknown initial configuration, starting from an arbitrary configuration

in which yarns inter-penetrate each other, and letting contact-friction interactions gradually separate these yarns until reaching the mechanical equilibrium. Geometrical features of this initial configuration are compared with measures on real samples and a good agreement is found. The model is then used to simulate tensile tests on braided ropes, and again good agreement with experimental data is obtained. The model can be used to study the influence of various design parameters on the mechanical response of the rope. It provides detailed information at the scale of individual yarns, which allows local phenomena taking place at this scale to be examined. In particular, load transfers between yarns due to friction, inducing heterogeneous distributions of stresses, are highlighted. The model developed is now being used to study more complex phenomena regarding braided synthetic ropes, and in particular the fatigue damage generated by repeated bending over sheaves. This work will be presented in a subsequent paper.

Acknowledgement

The authors gratefully acknowledge the contributions to this work of members of the French CITEPH project Lifetime of fibre ropes for deep sea handling.

[1] H.-C. Wu, M. H. Seo, S. Backer, J. F. Mandell, Structural modeling of double-braided synthetic fiber ropes, Textile research journal 65 (11) (1995) 619–631.

[2] S. R. Ghoreishi, P. Cartraud, P. Davies, T. Messager, Analytical modeling of synthetic fiber ropes subjected to axial loads. part i: A new con-

tinuum model for multilayered fibrous structures, International Journal of Solids and Structures 44 (9) (2007) 2924–2942.

[3] S. R. Ghoreishi, P. Davies, P. Cartraud, T. Messager, Analytical modeling of synthetic fiber ropes. part ii: A linear elastic model for 1+ 6 fibrous structures, International Journal of Solids and Structures 44 (9) (2007) 2943–2960.

[4] Y. Miao, E. Zhou, Y. Wang, B. A. Cheeseman, Mechanics of textile composites: Micro-geometry, Composites Science and Technology 68 (7) (2008) 1671–1678.

[5] N. Tolosana, M. Carrera, R. G. de Villoria, L. Castejon, A. Miravete, Numerical analysis of three-dimensional braided composite by means of geometrical modeling based on machine emulation, Mechanics of Advanced Materials and Structures 19 (1-3) (2012) 207–215.

[6] A. K. Pickett, J. Sirtautas, A. Erber, Braiding simulation and prediction of mechanical properties, Applied Composite Materials 16 (6) (2009) 345–364.

[7] D. Durville, A finite element approach of the behaviour of woven materials at microscopic scale, in: Mechanics of Microstructured Solids, Springer, 2009, pp. 39–46.

[8] D. Durville, Simulation of the mechanical behaviour of woven fabrics at the scale of fibers, International journal of material forming 3 (2) (2010) 1241–1251.

[9] D. Durville, 15 - microscopic approaches for understanding the mechanical behaviour of reinforcement in composites, in: P. Boisse (Ed.), Composite Reinforcements for Optimum Performance, Woodhead Publishing Series in Composites Science and Engineering, Woodhead Publishing, 2011, pp. 461 – 485.

[10] C. P. Laurent, P. Latil, D. Durville, R. Rahouadj, C. Geindreau, L. Orgéas, J.-F. Ganghoffer, Mechanical behaviour of a fibrous scaffold for ligament tissue engineering: Finite elements analysis *vs.* x-ray tomography imaging, Journal of the mechanical behavior of biomedical materials 40 (2014) 222–233.

[11] D. Durville, Contact-friction modeling within elastic beam assemblies: an application to knot tightening, Computational Mechanics 49 (6) (2012) 687–707.

[12] C. Leech, The modelling of friction in polymer fibre ropes, International Journal of Mechanical Sciences 44 (3) (2002) 621–643.

[13] P. Davies, Y. Reaud, L. Dussud, P. Woerther, Mechanical behaviour of hmpe and aramid fibre ropes for deep sea handling operations, Ocean Engineering 38 (17) (2011) 2208–2214.

[14] H. A. McKenna, J. W. S. Hearle, N. O'Hear, Handbook of fibre rope technology, Woodhead Publishing, 2004.